

# Impact of Vertex Functionalization on Flexibility of Porous Organic Cages

Jessica M. Rimsza,\* Sakun Duwal, and Harrison D. Root

Cite This: *ACS Omega* 2024, 9, 29025–29034

Read Online

ACCESS |



Metrics &amp; More

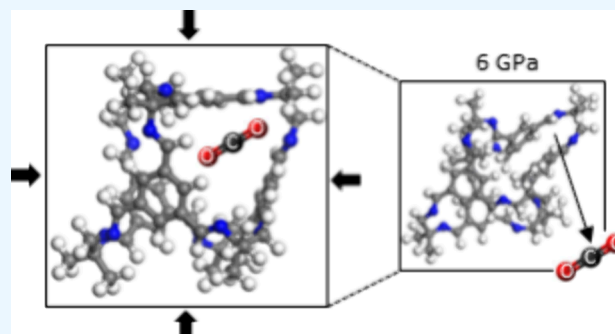


Article Recommendations



Supporting Information

**ABSTRACT:** Efficient carbon capture requires engineered porous systems that selectively capture CO<sub>2</sub> and have low energy regeneration pathways. Porous liquids (PLs), solvent-based systems containing permanent porosity through the incorporation of a porous host, increase the CO<sub>2</sub> adsorption capacity. A proposed mechanism of PL regeneration is the application of isostatic pressure in which the dissolved nanoporous host is compressed to alter the stability of gases in the internal pore. This regeneration mechanism relies on the flexibility of the porous host, which can be evaluated through molecular simulations. Here, the flexibility of porous organic cages (POCs) as representative porous hosts was evaluated, during which pore windows decreased by 10–40% at 6 GPa. POCs with sterically smaller functional groups, such as the 1,2-ethane in the CC1 POC resulted in greater imine cage flexibility relative to those with sterically larger functional groups, such as the cyclohexane in the CC3 POC that protected the imine cage from the application of pressure. Structural changes in the POC also caused CO<sub>2</sub> adsorption to be thermodynamically unfavorable beginning at ~2.2 GPa in the CC1 POC, ~1.1 GPa in the CC3 POC, and ~1.0 GPa in the CC13 POC, indicating that the CO<sub>2</sub> would be expelled from the POC at or above these pressures. Energy barriers for CO<sub>2</sub> desorption from inside the POC varied based on the geometry of the pore window and all the POCs had at least one pore window with a sufficiently low energy barrier to allow for CO<sub>2</sub> desorption under ambient temperatures. The results identified that flexibility of the CC1, CC3, or CC13 POCs under compression can result in the expulsion of captured gas molecules.



## 1. INTRODUCTION

Efficient CO<sub>2</sub> capture, particularly from dilute sources, requires highly tunable carbon capture materials with low-energy regeneration mechanisms. Amine scrubbing technology is currently the most common industrial process for CO<sub>2</sub> capture, which adsorbs CO<sub>2</sub> through chemisorption via formation of carbonate or carbamate phases.<sup>1</sup> The regeneration of aqueous amines requires the use of high temperatures to decompose the carbon-based phases, which accounts for 70–80% of the CO<sub>2</sub> capture cost.<sup>2</sup> Development of low energy regeneration mechanisms such as membrane vacuum regeneration have been evaluated but are still challenged by the strong chemisorption-based binding.<sup>3–5</sup> Materials with weaker physisorption binding would allow for low energy regeneration processes, but still require the high selectivity and gas capacity that are the primary benefits of amine-based technologies.

A potential material solution for these CO<sub>2</sub> capture challenges are porous liquids (PLs), composed of a solvated nanoporous host in a bulky solvent.<sup>6–8</sup> The solvent is limited from entering the interior pore space of the porous host, typically through steric effects.<sup>9</sup> Dissolved gases, such as CO<sub>2</sub>, are physisorbed either (i) inside the pore space of the nanoporous host or (ii) at the porous host–solvent interface.<sup>10</sup> Four types of PLs have been developed based on the

characteristics of the porous host or solvent.<sup>11</sup> Among these, Type 2 PLs are formed from the solvation of a single molecular cage structure, typically a porous organic cage (POC).

POCs are a class of nano- or microporous materials composed of discrete molecules with a single accessible pore.<sup>12–14</sup> Thousands of unique POCs have been developed with varying compositions and pore sizes that have allowed them to be used for capture and separation of CO<sub>2</sub>,<sup>15–17</sup> hydrogen isotopes,<sup>18,19</sup> and noble gases.<sup>20</sup> Additionally, the CC13 POC was a component of one of the first reported PLs in 2015<sup>6</sup> and has been subsequently used in preparation of Type 2 PLs.<sup>21</sup> Altering the POC in the PLs has resulted in size and shape selectivity for gas capture along with substantial increase in gas adsorption capacity.<sup>7,22,23</sup> For example, a Type 2 PL formed from an imine-based POC and a 15-crown-5 ether had an 8-fold increase in CH<sub>4</sub> adsorption over the neat

Received: May 7, 2024

Revised: June 5, 2024

Accepted: June 11, 2024

Published: June 19, 2024



liquid,<sup>6</sup> while the use of scrambled POCs in Type 2 PL doubled the amount of CH<sub>4</sub> adsorbed per POC.<sup>7</sup> The increase in gas uptake has been attributed to the number of gas binding sites introduced into the PL with the introduction of POCs,<sup>24</sup> as well as the additional pore space from the dissolved nanoporous host. The high gas capacity and tunability in a stable liquid-phase materials is a critical step toward development of efficient CO<sub>2</sub> capture materials to replace aqueous amines.

The presence of a POC inside a solvent system has potential benefits for CO<sub>2</sub> capture beyond an increase in the gas adsorption capacity. For example, efficient regenerable PLs may be possible through manipulation of the POC. Recently, some PLs have been found to exhibit compressibility based on infiltration of water molecules into ZIF-8E, a hydrophobic metal–organic framework (MOF) with retained reaction product, at pressures up to 10 GPa.<sup>25</sup> Structural changes occurred within the ZIF-8E nanoporous host during compression, attributed to the well-known gate-opening mechanism for water adsorption in ZIF-8.<sup>26</sup> In the water +ZIF-8E PL the hydrophobicity of the nanoporous host resulted in the compressibility of the PL, but this is just one possible mechanism of compressibility in PLs. An alternative is the collapse of the nanoporous host itself, and collapsible porous solids have been reported in literature with varying compositions.<sup>27–29</sup> In cases where steric exclusion of the solvent molecule causes permanent porosity in the PL composition, it may be that the pressure response of the nanoporous host is the driving factor controlling PL compressibility. Additionally, since adsorption of gas molecules inside the POC are sensitive to the pore geometry, changes to the porous host could alter the gas binding structures within the PL provided that the surrounding solvent molecules are still excluded.

Evaluation of structural flexibility of porous solids has focused on crystalline MOFs and POCs.<sup>30–32</sup> Here, molecular scale modeling evaluates how the composition of POCs affects their flexibility as an isolated cage molecule rather than in an extended structure. Three different POCs with varying vertex functionalization were simulated via density functional theory (DFT) to identify how the size and composition of the functionalization influence their flexibility. Single POC molecules were placed in periodic boxes, followed by compression to increase the POC–POC interaction under pressure. Changes in the bond lengths, bond angles, and pore window size were evaluated, along with stability of CO<sub>2</sub> binding in the interior porosity of the POC and changing activation energies for CO<sub>2</sub> adsorption. The results evaluated the flexibility of the POCs under pressure and the impact on the stability of CO<sub>2</sub> binding in the POCs that could be used to develop regenerable Type 2 PLs.

## 2. SIMULATION METHODS

Closed-shell projected-augmented wave (PAW) DFT calculations carried out using the Vienna Ab initio Simulations Package (VASP)<sup>33,34</sup> were used to evaluate POC flexibility. Similar methodologies evaluated molecular interactions with CC13 POCs, MOFs, and zeolites.<sup>19,35–41</sup> DFT calculations used a 500 eV cutoff along with the PBEsol exchange–correlation functional.<sup>42</sup> Van der Waals interactions were included with Grimme's D3 dispersion correction.<sup>43</sup> Structural optimizations used an electronic convergence criterion of 10<sup>–6</sup>

eV and a force convergence of 0.01 eV/Å. A  $\gamma$ -point  $k$ -point mesh and real-space algorithm were used for all calculations.

Three different imine-based POCs (CC1, CC3, and CC13) were evaluated with different vertex functionalizations. CC1 (C<sub>48</sub>H<sub>48</sub>N<sub>12</sub>) has 1,2-ethane, CC3 (C<sub>72</sub>H<sub>84</sub>N<sub>12</sub>) has cyclohexane, and CC13 (C<sub>60</sub>H<sub>72</sub>N<sub>12</sub>) has dimethyl functional groups at the vertices of the imine cage. These three POCs cover a range of vertex functional group sizes and are known POC compositions. Snapshots of the cage structures are included in Figure 1, and the total system sizes were 108 (CC1), 168 (CC3), and 114 (CC13) atoms.

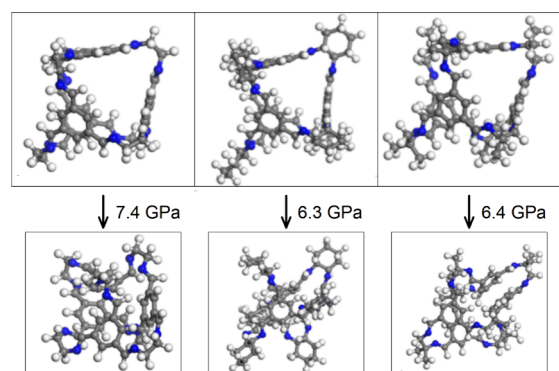


**Figure 1.** Snapshot of uncompressed (top) and compressed (bottom) POCs CC1 (left), CC3 (middle), and CC13 (right). Atom colors: carbon (gray), nitrogen (blue), hydrogen (white).

A single POC molecule was placed in a 25 × 25 × 25 Å simulation box and structurally optimized. Due to the presence of periodic boundary conditions, the effect is a simple cubic structure with ~ 10 Å separating the periodic images of the POC generating a gas-phase simulation cell. Use of isolated POC molecules to evaluate POC properties representative of bulk or nanocrystals has also been used by Miklitz et al.<sup>44</sup> and Jackson et al.<sup>45</sup> Then the volume of the box was decreased by decreasing each box length by 0.25 Å, followed by a full structural optimization without additional constraints. This compression–relaxation procedure was performed serially until the POC was interacting across the periodic boundary, increasing pressure within the simulation that mimics the application of external isostatic pressure. Compression of the simulation box continued until the final pressure was above 6 GPa. Based on the effective size of the POC, final box dimensions varied from 9.25 × 9.25 × 9.25 Å for CC1 to 10.50 × 10.50 × 10.50 Å for CC3. A single simulation was performed for the POC composition. Note that there is no covalent bonding across the periodic boundaries and that POC–POC interactions are through noncovalent mechanisms. The compression procedure used here does not replicate crystallization conditions and bulk POC systems have known crystal structures, including monoclinic C2/c for the CC1 POC,<sup>12</sup> cubic F4<sub>1</sub>32 for the CC3 POC,<sup>12</sup> and trigonal P3 for the CC13 POC.<sup>46</sup> Rather, the procedure replicates conditions in which the concentration of individual POCs is sufficiently high to allow for a direct POC–POC interaction. Given the limited system size and lack of thermal effects in these simulations, evaluation of how the high concentration of POCs may affect rheological properties of the PL was not evaluated. Structural analysis of the POCs was performed using the postprocessing software R.I.N.G.S.<sup>47</sup> Initial POC structures in

the  $25 \times 25 \times 25 \text{ \AA}$  box and the final structures at maximum pressure are included in the Supporting Information.

For compressed POCs, a  $\text{CO}_2$  molecule was placed in the internal porosity of the POC, and the simulation was optimized while keeping the POC structure frozen. This ensured that the POC did not expand during the optimization.  $\text{CO}_2$  binding energies were calculated based on differences in the electronic energy of the system ( $E_{\text{CO}_2+\text{POC}}$ ), the single point electronic energy of the POC after the  $\text{CO}_2$  was removed ( $E_{\text{POC}}$ ), and the electronic energy of a  $\text{CO}_2$  ( $E_{\text{CO}_2}$ ) in the center of a  $25 \times 25 \times 25 \text{ \AA}$  box as outlined in eq 1. Electronic energies have been used to describe the binding strength and probability in a variety of porous materials.<sup>35,48–50</sup>

$$E_B = E_{\text{CO}_2+\text{POC}} - \sum (E_{\text{CO}_2} + E_{\text{POC}}) \quad (1)$$

In addition to the  $\text{CO}_2$  binding configuration inside the POC,  $\text{CO}_2$  was placed outside the POC at a distance of  $\sim 3 \text{ \AA}$ . Four  $\text{CO}_2$  locations outside each of the four pore windows were evaluated outside to account for variations in the pore window size during optimization. The two  $\text{CO}_2$  binding sites, one inside and one outside the POC were used as the end points in climbing-image nudged-elastic-band (NEB)<sup>51,52</sup> calculations to identify the activation energy for the  $\text{CO}_2$  to enter the POC. These NEB simulations identified the minimum energy path between the initial and final states, with the transition state (or saddle point) identified as the highest energy structure along the minimum energy path. NEB simulations used the same parameters as the static DFT calculations including exchange-correlation functional, basis set, dispersion correction, and energy cutoff. Five snapshots were generated along the minimum energy path, and NEB calculations used a spring coefficient of 0.05. NEB calculations have been successful in calculating activation energies across a variety of systems, including in solid-state porous materials.<sup>53,54</sup>

### 3. RESULTS

**a. Effective POC Particle Size.** Isostatic compression of the POC was achieved by decreasing the simulation box size, forcing the POC to interact with periodic replicates. Through this process the total system energy increases from initially noninteracting particles, to packed particles, and finally to compressed particles. Changes in the energy of the POC as the cell size decreases is included in Figure 2, with the system energies referenced to the initial energy of the POC. The energies are fit to a Lennard–Jones (L–J) potential that describes the interactions of electronically neutral atoms or molecules. The L–J potential is based on the distance between particles ( $r$ ), the dispersion energy ( $\epsilon$ ), and the distance where the particle–particle potential energy ( $V$ ) is zero ( $\sigma$ ), as seen in eq 2.

$$V(r) = 4\epsilon \left[ \left( \frac{\sigma}{r} \right)^{12} - \left( \frac{\sigma}{r} \right)^6 \right] \quad (2)$$

Based on the L–J fit of the change in energy and box size data in Figure 2, the strongest POC–POC interactions occur for the CC3 POC ( $\epsilon = 1.53 \text{ eV}$ ), while the CC1 and CC13 POCs have weaker interactions ( $\epsilon = 1.03$  and  $1.00 \text{ eV}$ , respectively). Additionally, the CC1 POC has the tightest packing density, with a  $\sigma$  value of  $10.21 \text{ \AA}$  compared with  $11.25 \text{ \AA}$  for the CC13 POC and  $11.42 \text{ \AA}$  for the CC3 POC. The  $\sigma$  value indicates for what cell size the POC–POC interactions generate a positive

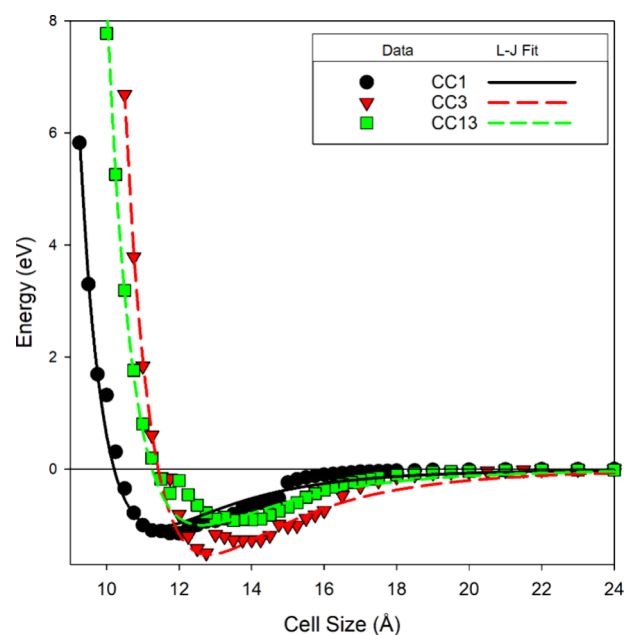


**Figure 2.** Change in energy (eV) will affect cell size (Å) for the three different POCs studied. Data are fit with a Lennard–Jones (L–J) potential (eq 1).

isostatic pressure and is the basis for further structural analysis of the POCs under compression. Plots of isostatic pressure versus change in energies (Figure S1) and pressure versus cell size (Figure S2) for the three POCs are included in the Supporting Information.

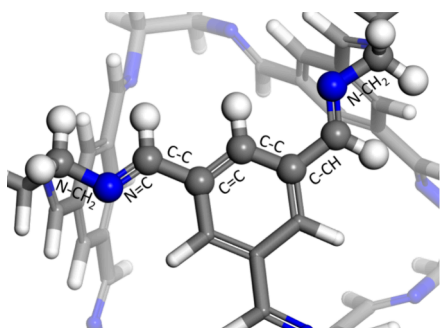
**b. Structural Evolution of POCs under Isostatic Compression.** Isostatic compression results in significant structural changes across all three POCs studied, as shown in Figure 1. Evaluation of interatomic bonding identified that while the structure of the POCs changed, no breaking or formation of bonds occurred. Instead, structural changes were through compression or expansion of interatomic distances and bond angles. To quantify this effect, changes in the C–C and N–C bond lengths were evaluated as a function of isostatic pressure across the three POCs, as seen in Table 1, with bond locations noted in Figure 3. Bond lengths on average exhibited compression of  $< 0.01 \text{ \AA}$  up to 6 GPa. The exception is the N=C double bond along the edge of the POC, which undergoes a slight expansion by  $0.001\text{--}0.006 \text{ \AA}$ . The N=C bonds are the strongest bond in the POC, with a bond energy of  $6.37 \text{ eV}$ , compared with C–C ( $3.59 \text{ eV}$ ) and N–C ( $3.16 \text{ eV}$ ), causing the slight expansion. The only bond in the system of comparable strength is the C=C bond ( $6.36 \text{ eV}$ ) that is protected within the benzene ring in the linker and does not experience the same force as bonds located at the vertices of the POC.

Similarly, the C–C–C and N–C–C interatomic bond angles (Table 2) also experience compression as the pressure increases. The change in the bond angle is  $< 1.0^\circ$  over the entire pressure range. In all three of the POC structures one bond angle exhibits the opposite trend, expanding instead of contracting. For the CC1 and CC13 POCs the C–N=C bond angle increases slightly, by  $0.8^\circ$  and  $1.4^\circ$  respectively. Since these bond angles incorporate the strong N=C bond that expand during compression this accounts for the expansion of the C–N=C bond angle over the same pressure range. In contrast, in the CC3 POC it is the N–C–C bond angle that



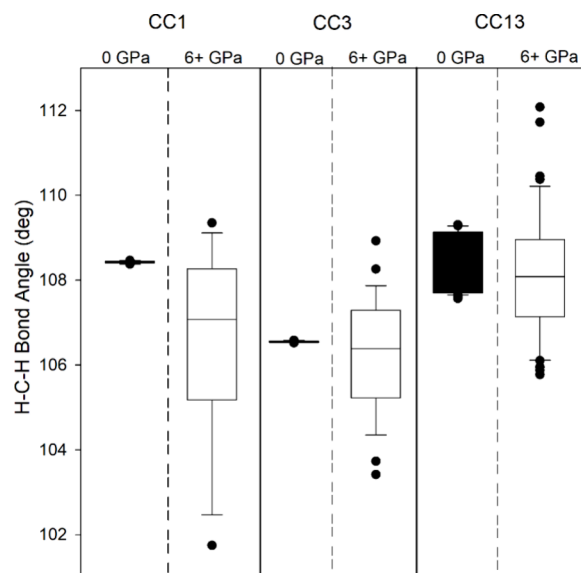
**Table 1. Weighted Average of the C–C and N–C Bonds in the POC Structures during Isostatic Compression from 0.0 GPa to 6.0+ GPa**

pressure (GPa)	C=C (Å)		C–C (Å)		C–CH (Å)		N=C (Å)		N–CH <sub>2</sub> (Å)	
	0	6+	0	6+	0	6+	0	6+	0	6+
CC1	1.399	1.391	1.465	1.453	1.529	1.512	1.274	1.275	1.437	1.428
CC3	1.398	1.391	1.465	1.462	1.527	1.515	1.275	1.281	1.440	1.433
CC13	1.398	1.392	1.466	1.452	1.533	1.525	1.274	1.277	1.444	1.437

**Figure 3.** Snapshot of the CC1 POC with interatomic bond distances labeled. Atom colors: nitrogen (blue), carbon (gray), and hydrogen (white).

expands by 0.9°. In the CC3 POC, the N–C–C bond angle connects the linkers to the cyclohexane functional group, which is sterically bulkier and more sensitive to packing than the sterically smaller functional groups on the CC1 and CC13 POCs.

Analysis of the structural changes in the functional groups of the POCs, rather than the entire cage structure, was used to identify the impact of pressure on the functional group, with the data included in Figures 4 and 5. For the CC1 POC, the C–C bond and the H–C–H bond angle at the edge of the POC contract slightly under compression from 1.528 Å and 108.4° at 0 GPa to 1.515 Å and 106.7° at 6+ GPa, along with larger standard deviations. These results indicate that the H–C–H bond angle is both contracting and expanding during the application of isostatic compression, based on the 8° difference between the maximum and minimum H–C–H angles. The variability in the H–C–H bond angle and C–C bond distance on the vertex of the POC is strongest for the CC1 POC, which does not contain the bulkier dimethyl (CC13) or cyclohexyl (CC3) functional groups. For example, CC3, which has the sterically largest vertex functionalization, has no change in the average C–C distance from 0 to 6 GPa and only a 0.3° variation in the H–C–H bond angles on the cyclohexyl moiety. Instead, the C–C=C bonds within the cyclohexyl functional group vary from 111.0 ± 0.6° at 0 GPa to 110.7 ± 3.5° at 6 GPa. Therefore, the application of isostatic pressure is causing distortion of the cyclohexyl functional group rather than variation in the imine cage of the POC. Similarly, in the CC13 POC the C–C–C bond angle formed between the two

**Figure 4.** Distribution of H–C–H bond angles in vertex functional groups in the POC structures during isostatic compression from 0.0 GPa to 6.0+ GPa.

dimethyl groups increases from 110.3 ± 0.0° to 110.6 ± 7.9°. The variation in the C–C–C bond angle between the two dimethyl groups suggests that the compression is unequal. Sterically large functional groups exacerbate this effect, which affects POC packing and pressure responses.

**c. Pore Window Changes in POCs.** While the POCs exhibit minimal changes in the bond distances during compression, it is clear from Figure 1 that the structure of the POC is changing. Therefore, changes in the POC structure arise not from compression or expansion of individual bonds but from changes in the bond and dihedral angles of the POC. Among the POC structural descriptors, changes in the pore window size are of particular interest for applications in gas capture, since the geometry of the pore window controls diffusion of gases into and out of the POC. The size of the pore window was calculated based on the two nitrogen atoms located at the vertices of the POC. The midpoint between the two nitrogen atoms were used to identify the edges of the triangle shaped windows in the POC to calculate the pore window size. A schematic of the pore window in the CC1 POC is included in the Supporting Information as Figure S3. The

**Table 2. Weighted Average of C–C–C and N–C–C Interatomic Angles in the POC Structures during Isostatic Compression from 0.0 GPa to 6.0+ GPa.**

pressure (GPa)	C–C–C (°)		N–C–C (°)		N=C–C (°)		C–N–C (°)	
	0	6+	0	6+	0	6+	0	6+
CC1	118.1	117.7	108.3	107.7	120.7	120.3	115.7	116.5
CC3	114.2	113.7	107.3	108.2	121.0	120.0	115.8	115.7
CC13	115.2	114.9	107.0	106.0	119.5	119.2	117.3	118.7

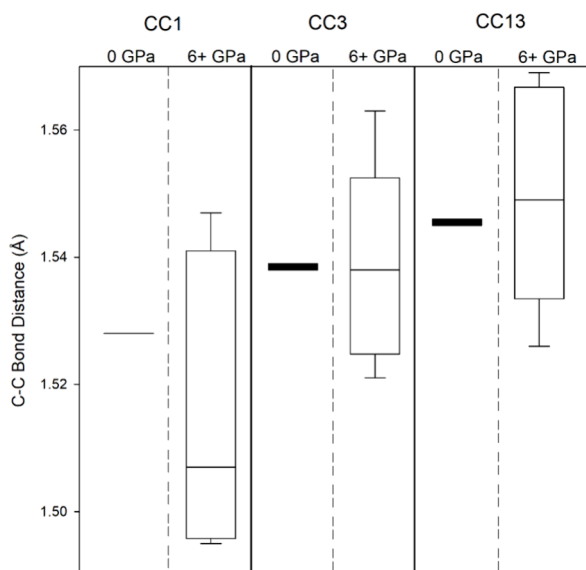


**Figure 5.** Distribution of C–C bond distances in vertex of the POC structures during isostatic compression from 0.0 GPa to 6.0+ GPa.

sizes of the four pore windows on each POC are plotted in Figure 6 as a function of pressure. As the pressure increases the pore windows universally contract from an initial value of  $\sim 26 \text{ \AA}^2$  to final values between  $21.8 \pm 1.7 \text{ \AA}^2$  (CC3) and  $19.9 \pm 2.9 \text{ \AA}^2$  (CC1), with the CC1 POC exhibiting the most overall compression at 23.3%. Initially, the CC13 POC had the strongest response to pressure, with an average pore window size decreasing from  $25.2 \pm 0.4 \text{ \AA}^2$  to  $22.7 \pm 1.4 \text{ \AA}^2$  as the pressure increases to 1 GPa or 10.1% compression. Over the same pressure range, up to 1 GPa, the average pore window contracted by only 7.4% for CC1 and 6.5% for CC3. Over the pressure range from 1 to 6 GPa, the pore window size decreased significantly for the CC1 POC, while for the CC3 and CC13 POCs the pore window size stays more consistent. The size of the functional group on the vertex of the CC1 POC allows the imine cage to contract more at higher pressures, while the larger functional groups for the CC3 and CC13 POCs protect the imine cage from exhibiting the same amount of compression.

Additionally, at higher pressures, the pore windows do not compress equally, as seen in Figure 6. Unequal compression of the pore windows is unexpected, since all the windows in the POC are chemically equivalent. Individual changes in the pore window are included in Table 3. Note that the naming convention A, B, C, and D is used to identify individual pore windows.

The CC1 POC exhibited the widest variation of the pore window size in response to pressure with pore windows decreasing by 16.7–35.4%. In contrast, the CC3 and CC13 POCs have an overall smaller change in the pore window size of only  $14.7 \pm 5.5\%$  and  $15.6 \pm 1.8\%$ , respectively. Additionally, for the CC3 POC two of the four pore windows had significantly different changes in the pore window size relative to the median. The size of pore window A decreased by 8.0% during compression compared to 23.2% for pore window D. Finally, for the CC13 POC all of the pore windows compressed relatively consistently.

#### d. Predicted Gas Adsorption in Compressed POCs.

Compression of POCs alters the geometry of the pore, changing its ability to capture gas molecules.  $\text{CO}_2$  gas binding

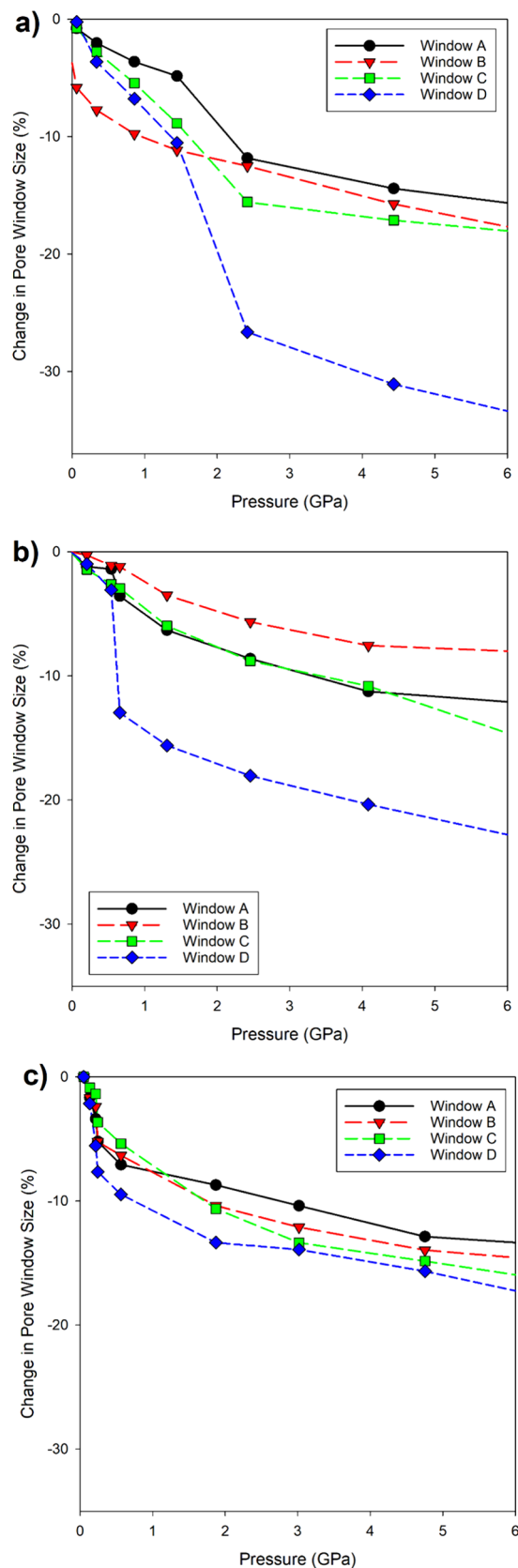


**Figure 6.** Changes in pore windows of (a) CC1, (b) CC3, and (c) CC13 POCs as a function of the pressure. Data are separated by pore window (A–D) and naming is consistent with Table 3 and Figure 8.

**Table 3.** Change in the pore window (%) from 0.0 GPa to 6+ GPa for the CC1, CC3, and CC13 POCs. Data are separated by pore window (A-D) and naming is consistent with Figure 6 and Figure 8.

POC	window A (%)	window B (%)	window C (%)	window D (%)	avg (%)
CC1	19.4	16.7	35.4	18.8	22.6 ± 7.5
CC3	8.0	23.2	15.3	12.2	14.7 ± 5.5
CC13	14.7	18.4	13.5	15.6	15.6 ± 1.8

energies inside the POCs as a function of isostatic pressure were calculated and included in Figure 7. Overall, as the

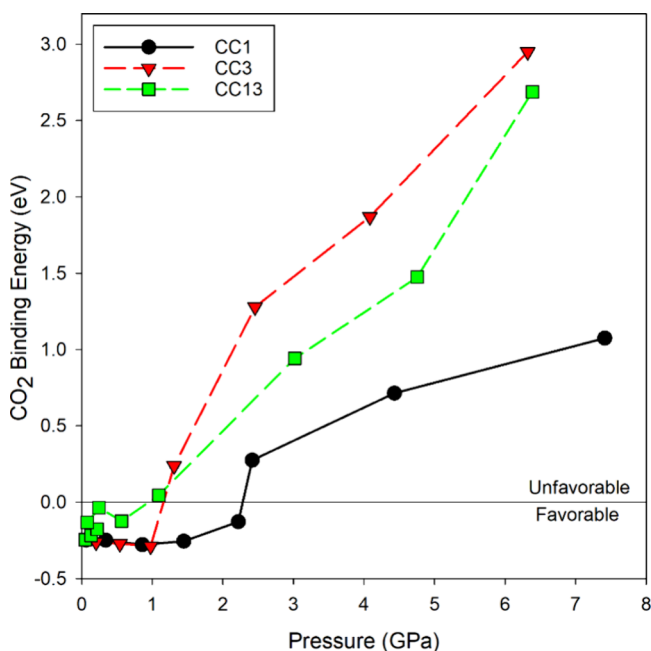


**Figure 7.** CO<sub>2</sub> binding energies inside the POC as a function of the isostatic pressure. Favorable binding energies are negative, while unfavorable binding energies are positive.

pressure on the POCs increased, the CO<sub>2</sub> binding energies inside the POC become unfavorable, indicated by a positive binding energy. Simultaneously, the internal porosity of the POC decreases with pressure, as seen in Figure S4. Practically, CO<sub>2</sub> would be expected to desorb from the interior pore space once the binding energy becomes unfavorable. For the CC1 POC, this occurs at 2.3 GPa, compared to 1.2 GPa for the CC3 POC, and 1.0 GPa for the CC13 POC. These results indicate that the CC1 POC has a more rigid structure that is less sensitive to the application of pressure than the CC3 and CC13 POCs. Additionally, this is opposite to the trend seen in the changing structure of the functional group under compression. The CC1 POC contains the 1,2-ethane functional group that exhibited the least variation in the H–C–H bond angles, compared to the C=C bond angles in the cyclohexane functional group in the CC3 POC and the dimethyl functional group in the CC13 POC. These results indicate that the structural changes in the functional groups influence the stability of the POC, causing the variation in the CO<sub>2</sub> binding energies.

#### e. Prediction of CO<sub>2</sub> Infiltration in Compressed POCs.

Adsorption of CO<sub>2</sub> in POCs requires not just a stable binding site inside the POC, but also the ability to diffuse through a pore window. Past studies on mechanisms of gas infiltration into nanoporous hosts in PLs have identified size and shape selectivity based on the geometry of the nanoporous host<sup>20,55</sup>

as well as multistep mechanism of adsorption based on cooperative interactions between the gas molecule and the pore window.<sup>56,57</sup> Our NEB analysis identifies how the geometry of the pore window changes the activation energy for POC infiltration by CO<sub>2</sub>. NEB calculations move the CO<sub>2</sub> through the pore window to identify the energy barrier for molecular infiltration. The energy values are referenced to the binding energy of the CO<sub>2</sub> inside the POC (reaction coordinate 0) with a final position outside the POC (reaction coordinate 6). To keep the POC from expanding back to its original structure during the NEB calculations, the locations of the POC atoms were fixed, while the CO<sub>2</sub> was simulated without constraint. Snapshots of a CO<sub>2</sub> exiting the CC13 POC through pore window A following isostatic compression of the POC is included in Figure S5.

As seen in Figure 8, all the POCs evaluated had nearly activation less energy barriers for the initial POC structure (black line), indicating that the CO<sub>2</sub> would freely diffuse into the POC. In contrast, when the POC is under isostatic compression energy barriers exist for CO<sub>2</sub> exiting the POC. For instance, in the CC3 POC the activation energy barriers for CO<sub>2</sub> to exit the POC range from 0.2 eV for window A to 4.4 eV for window D. Low activation energy barriers, typically <0.5 eV, could be overcome with entropic effects so that the CO<sub>2</sub> could exit the interior pore space under ambient temperatures. For larger activation energy barriers, those >0.5 eV, the pore window is so distorted that the CO<sub>2</sub> could not exit the pore. In all three of the POCs, two of the four pore windows are still available for CO<sub>2</sub> desorption, even at high pressures. Additionally, NEB calculations for CO<sub>2</sub> desorption in the CC1 POC through pore window B, in the CC3 POC through pore window D, and in the CC13 POC through pore window D as a function of pressure are included in the Supporting Information as Figure S6. As the pressure increases, the activation energy for CO<sub>2</sub> desorption slightly increases to ~0.2 eV for pressures between 0.5 and 1.5 GPa, followed by a sharp drop to an activationless process. In comparison, the analysis of pore window D in the CC13 POC indicates a continuously increasing barrier for CO<sub>2</sub> desorption. Practically, this indicates that under isostatic pressure, molecules inside the POCs are not trapped during compression, but instead can exit through one of the two pore windows with minimal energy barriers.

## 4. DISCUSSION

The flexibility of single POC molecules under compression were evaluated using DFT simulations, which is distinct from their bulk crystalline properties. Generally, in crystalline experimental systems, the rigidity arises from an extended structure with preferred orientations. In this study, the results evaluate the rigidity of the isolated POC molecule, rather than of a bulk crystal structure. By isolating the POC we have focused on which bond angles in the POC exhibit variation under compression and on the role of the vertex functionalization on these behaviors.

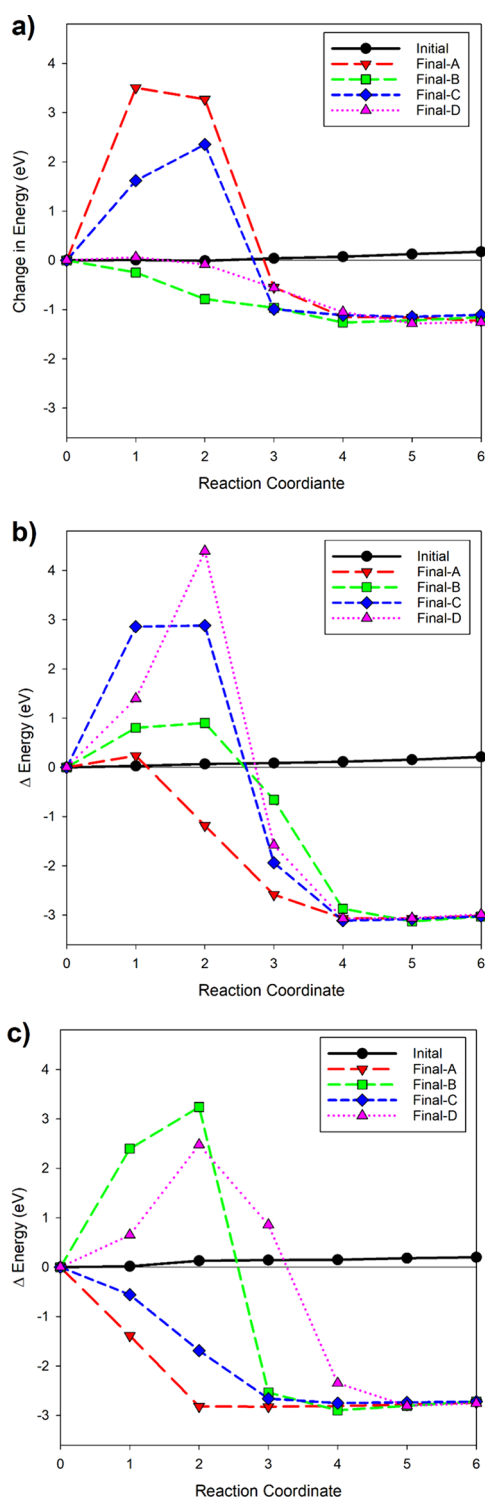


**Figure 8.** Nudged-elastic-band calculations of CO<sub>2</sub> desorption from the interior of the (a) CC1, (b) CC3, and (c) CC13 POC. Reaction coordinate 0 occurs when the CO<sub>2</sub> is inside the POCs, and the reaction coordinate 6 is when the CO<sub>2</sub> is outside the interior pore space. Data are separated by a pore window (A–D), and naming is consistent with Table 3 and Figure 6.

Overall, the results indicate that the average bond distance and bond angles in the POC structures exhibit limited sensitivity to the application of isostatic pressure, which is primarily manifested as a compression of these structural descriptors. Compression of bond angles, rather than bond

breakage or formation, also suggests that the observed structural changes would be reversible if the pressure was removed. The lack of reactivity is encouraging for the use of isostatic compression as a regeneration mechanism, though evaluation of reactivity of the POC–solvent interface under compression will need to be evaluated in future studies.

Pressure effects on the POC structure are more significant for the large asymmetric vertex functional groups (for example, in the CC3 POC), demonstrated by a larger variation in their bond angles at higher pressures. Additionally, the aggregate effect of these structural changes may influence the binding energies that control gas uptake and infiltration of the POC.

Influence of the pressure on the pore window was evaluated to identify if a gas molecule would be trapped inside the POC during compression. Significant variation in the compression of the pore window was found, indicating that asymmetric effects occurring due to POC–POC interactions. The CC1 and CC3 POCs with symmetric functional groups had two pore windows that preferentially compressed, window A and window C for the CC1 POC and window A and window D for the CC3 POC. Conversely, the CC13 POC with asymmetric functionalization with two methyl groups located on one corner of the 1,2-ethane terminus of the imine cage resulted in consistent compression of the pore window. The size of the pore window controls the accessibility of the interior of the POC for gas capture, and POCs containing pore windows that respond inconsistently to pressure may affect the gas capture selectivity of the compressed POC.

The variation in the vertex functionality of the POC influences the binding of CO<sub>2</sub> in the POC during the application of pressure. For the CC1 and CC3 POCs, which have symmetric vertex functionalization, the binding energy for CO<sub>2</sub> in the POC is consistent at  $\sim 0.25$  eV until a sudden change to an unfavorable binding energy is observed at sufficiently high pressures. In contrast, the CC13 POC, with an asymmetric dimethyl vertex functionalization, has a gradual response to pressure, as seen in Figure 7. For the CC13 POC even isostatic pressures of  $< 0.2$  GPa cause a change in the CO<sub>2</sub> binding energy in the POC. This trend is not strictly linear with increasing pressure. For instance, at isostatic pressures of 0.06 and 0.24 GPa there are weaker CO<sub>2</sub> binding energies in the interior pore space compared with higher-pressure conditions (0.57 GPa). The packing of the CC13 POC with itself is not as ordered as in the CC1 and CC3 POCs, and rotation of the POC can introduce variations in the pressure response. These results would also vary if the POC adopted the preferred crystal structure during compression, which is not necessarily cubic. Finally, in PLs the potential for solvent infiltration of the POC under pressure and the reactivity of the POC–solvent interface will need to be evaluated to fully understand the potential of POC flexibility as a source of regenerable PLs.

## 5. CONCLUSION

POCs flexibility was evaluated using DFT simulations to explore the ability to regenerate POC-based PLs via the application of isostatic pressure. Three different POCs were evaluated, CC1, CC3, and CC13, to account for varying functionalizations of the imine-based cages. POCs underwent isostatic compression by decreasing the simulation box, forcing the POC to interact with its periodic images and creating intermolecular pressures up to 6 GPa. Limited changes in the interatomic bonds and angles occurred during compression.



Structural changes in the POC were more apparent in the pore windows, which contracted by 10–40% as the pressure increased. The CC1 POC exhibited the greatest compression of the pore windows due to the smaller functional groups (1,2-ethane) that resulted in greater compression of the imine cage relative to the CC3 (cyclohexane) and CC13 (dimethyl) POCs. At zero pressure, CO<sub>2</sub> capture was favorable in all the POCs, but as the pressure increases, CO<sub>2</sub> binding becomes thermodynamically unfavorable at ~2.2 GPa for the CC1 POC, ~1.1 GPa for the CC3 POC, and ~1.0 GPa for the CC13 POC. Under these pressure regimes, the CO<sub>2</sub> would be expelled from the POC. Energy barriers for CO<sub>2</sub> desorption from the POC varied based on the compression of the pore window, but at 6 GPa all the POCs had at least one pore window with a sufficiently low energy barrier to allow for CO<sub>2</sub> desorption under ambient temperatures. Further studies on POC-containing PLs under compression, including POC–solvent combinations, would provide additional insight into how pressure could cause infiltration of the POC or reactivity at the POC–solvent interface are currently being pursued. Ultimately, regeneration of PLs containing CC1, CC3, and CC13 POCs may be accomplished pending ongoing studies on solvent infiltration and PL stability.

## ■ ASSOCIATED CONTENT


### SI Supporting Information

The Supporting Information is available free of charge at <https://pubs.acs.org/doi/10.1021/acsomega.4c04186>.


The change in energy versus pressure (Figure S1) and pressure versus cell size (Figure S2) for the POCs during isostatic compression; A schematic of the methodology used for calculation of the pore window size (Figures S3); Changes in the internal pore volume of the POC with increased pressure (Figure S4); Snapshots of a CO<sub>2</sub> exiting the CC13 POC through Window A following compression (Figure S5): Nudged-elastic band calculations of CO<sub>2</sub> desorption from the interior of the POCs at varying pressures (Figure S6); Atomic coordinates for the compressed and uncompressed POC structures (PDF)

## ■ AUTHOR INFORMATION

### Corresponding Author

Jessica M. Rimsza – *Geochemistry Department, Sandia National Laboratories, Albuquerque, New Mexico 87123, United States*;  [orcid.org/0000-0003-0492-852X](https://orcid.org/0000-0003-0492-852X);  
Email: [jrimsza@sandia.gov](mailto:jrimsza@sandia.gov)

### Authors

Sakun Duwal – *Dynamic Material Properties Department, Sandia National Laboratories, Albuquerque, New Mexico 87123, United States*;  [orcid.org/0000-0002-0254-1615](https://orcid.org/0000-0002-0254-1615)  
Harrison D. Root – *Advanced Materials Laboratory, Sandia National Laboratories, Albuquerque, New Mexico 87123, United States*

Complete contact information is available at:  
<https://pubs.acs.org/doi/10.1021/acsomega.4c04186>

### Author Contributions

J.M.R.: Conceptualization, Formal analysis, Methodology, Project administration, Funding acquisition, Writing—original draft, Writing—review and editing. S.D.: Conceptualization;

Funding acquisition, Writing—review and editing. H.R.: Conceptualization, Funding acquisition, Writing—review and editing.

### Notes

The authors declare no competing financial interest.

## ■ ACKNOWLEDGMENTS

The authors would like to thank Matthew S. Christian (Sandia National Laboratories) for helpful discussions. This work was performed with support from the Sandia National Laboratories Laboratory Research and Development (LDRD) program under Project #230709 and from the Center for Understanding and Controlling Accelerated and Gradual Evolution of Materials for Energy (UNCAGE-ME), an Energy Frontier Research Center funded by the U.S. Department of Energy, Office of Science, Office of Basic Energy Sciences, under Award No. DE-SC0012577. This article has been authored by an employee of National Technology and Engineering Solutions of Sandia, LLC under Contract No. DE-NA0003525 with the U.S. Department of Energy (DOE). The employee owns all right, title and interest in and to the article and is solely responsible for its contents. The United States Government retains and the publisher, by accepting the article for publication, acknowledges that the United States Government retains a nonexclusive, paid-up, irrevocable, worldwide license to publish or reproduce the published form of this article or allow others to do so, for United States Government purposes. The DOE will provide public access to these results of federally sponsored research in accordance with the DOE Public Access Plan <https://www.energy.gov/downloads/doe-public-access-plan>.

## ■ REFERENCES

- (1) Meng, F.; Meng, Y.; Ju, T.; Han, S.; Lin, L.; Jiang, J. Research progress of aqueous amine solution for CO<sub>2</sub> capture: A review. *Renew. Sustain. Energy Rev.* **2022**, *168*, 112902.
- (2) Nwaoha, C.; Idem, R.; Supap, T.; Saiwan, C.; Tontiwachwuthikul, P.; Rongwong, W.; Al-Marri, M. J.; Benamor, A. Heat duty, heat of absorption, sensible heat and heat of vaporization of 2-Amino-2-Methyl-1-Propanol (AMP), Piperazine (PZ) and Monoethanolamine (MEA) tri-solvent blend for carbon dioxide (CO<sub>2</sub>) capture. *Chem. Eng. Sci.* **2017**, *170*, 26–35.
- (3) Vadillo, J. M.; Díaz-Sainz, G.; Gómez-Coma, L.; Garea, A.; Irabien, A. Chemical and physical ionic liquids in CO<sub>2</sub> capture system using membrane vacuum regeneration. *Membranes* **2022**, *12* (8), 785.
- (4) Wang, Z.; Fang, M.; Pan, Y.; Yan, S.; Luo, Z. Comparison and selection of amine-based absorbents in membrane vacuum regeneration process for CO<sub>2</sub> capture with low energy cost. *Energy Procedia* **2013**, *37*, 1085–1092.
- (5) Yan, S.; Fang, M.; Luo, Z.; Cen, K. Regeneration of CO<sub>2</sub> from CO<sub>2</sub>-rich alkanolamines solution by using reduced thickness and vacuum technology: Regeneration feasibility and characteristic of thin-layer solvent. *Chem. Eng. Process.: Process Intensif.* **2009**, *48* (1), 515–523.
- (6) Giri, N.; Del Pópolo, M. G.; Melaugh, G.; Greenaway, R. L.; Rätzke, K.; Koschine, T.; Pison, L.; Gomes, M. F. C.; Cooper, A. I.; James, S. L. Liquids with permanent porosity. *Nature* **2015**, *527* (7577), 216–220.
- (7) Greenaway, R. L.; Holden, D.; Eden, E. G.; Stephenson, A.; Yong, C. W.; Bennison, M. J.; Hasell, T.; Briggs, M. E.; James, S. L.; Cooper, A. I. Understanding gas capacity, guest selectivity, and diffusion in porous liquids. *Chem. Sci.* **2017**, *8* (4), 2640–2651.
- (8) Li, Y. Research progress of porous liquids. *ChemistrySelect* **2020**, *5* (43), 13664–13672.



- (9) O'Reilly, N.; Giri, N.; James, S. L. Porous liquids. *Chem. Eur. J.* **2007**, *13* (11), 3020–3025.
- (10) Rimsza, J. M.; Nenoff, T. M. Porous Liquids: Computational Design for Targeted Gas Adsorption. *ACS Appl. Mater. Interfaces* **2022**, *14* (16), 18005–18015.
- (11) Bennett, T. D.; Coudert, F.-X.; James, S. L.; Cooper, A. I. The changing state of porous materials. *Nat. Mater.* **2021**, *20* (9), 1179–1187.
- (12) Tozawa, T.; Jones, J. T.; Swamy, S. I.; Jiang, S.; Adams, D. J.; Shakespeare, S.; Clowes, R.; Bradshaw, D.; Hasell, T.; Chong, S. Y.; et al. Porous organic cages. *Nat. Mater.* **2009**, *8* (12), 973–978.
- (13) Hasell, T.; Cooper, A. I. Porous organic cages: soluble, modular and molecular pores. *Nat. Rev. Mater.* **2016**, *1* (9), 1–14.
- (14) Briggs, M. E.; Cooper, A. I. A perspective on the synthesis, purification, and characterization of porous organic cages. *Chem. Mater.* **2017**, *29* (1), 149–157.
- (15) Krishnan, K.; Crawford, J. M.; Thallapally, P. K.; Carreon, M. A. Porous Organic Cages CC3 and CC2 as Adsorbents for the Separation of Carbon Dioxide from Nitrogen and Hydrogen. *Ind. Eng. Chem. Res.* **2022**, *61* (29), 10547–10553.
- (16) Hasell, T.; Armstrong, J. A.; Jelfs, K. E.; Tay, F. H.; Thomas, K. M.; Kazarian, S. G.; Cooper, A. I. High-pressure carbon dioxide uptake for porous organic cages: comparison of spectroscopic and manometric measurement techniques. *Chem. Commun.* **2013**, *49* (82), 9410–9412.
- (17) Li, Z. J.; Srebnik, S. Expanding carbon capture capacity: uncovering additional CO<sub>2</sub> adsorption sites in imine-linked porous organic cages. *Phys. Chem. Chem. Phys.* **2021**, *23* (17), 10311–10320.
- (18) Liu, M.; Zhang, L.; Little, M. A.; Kapil, V.; Ceriotti, M.; Yang, S.; Ding, L.; Holden, D. L.; Balderas-Xicohtencatl, R.; He, D.; et al. Barely porous organic cages for hydrogen isotope separation. *Science* **2019**, *366* (6465), 613–620.
- (19) Vogel, D. J.; nenoff, T.; Rimsza, J. Design Elements for Enhanced Hydrogen Isotope Separations in Barely Porous Organic Cages. *ACS Omega* **2022**, *7* (9), 7963.
- (20) Chen, L.; Reiss, P. S.; Chong, S. Y.; Holden, D.; Jelfs, K. E.; Hasell, T.; Little, M. A.; Kewley, A.; Briggs, M. E.; Stephenson, A.; et al. Separation of rare gases and chiral molecules by selective binding in porous organic cages. *Nat. Mater.* **2014**, *13* (10), 954–960.
- (21) Borne, I.; Saigal, K.; Jones, C. W.; Lively, R. P. Thermodynamic Evidence for Type II Porous Liquids. *Ind. Eng. Chem. Res.* **2023**, *62* (29), 11689–11696.
- (22) Lai, B.; Cahir, J.; Tsang, M. Y.; Jacquemin, J.; Rooney, D.; Murrer, B.; James, S. L. Type 3 porous liquids for the separation of ethane and ethene. *ACS Appl. Mater. Interfaces* **2021**, *13* (1), 932–936.
- (23) Jie, K.; Zhou, Y.; Ryan, H. P.; Dai, S.; Nitschke, J. R. Engineering permanent porosity into liquids. *Adv. Mater.* **2021**, *33* (18), 2005745.
- (24) Yin, J.; Zhang, J.; Wang, C.; Lv, N.; Jiang, W.; Liu, H.; Li, H.; Zhu, W.; Li, H.; Ji, H. Theoretical insights into CO<sub>2</sub>/N<sub>2</sub> selectivity of the porous ionic liquids constructed by ion-dipole interactions. *J. Mol. Liq.* **2021**, *344*, 117676.
- (25) Lai, B.; Liu, S.; Cahir, J.; Sun, Y.; Yin, H.; Youngs, T.; Tan, J. C.; Fonrouge, S. F.; Pópolo, M. G. D.; Borioni, J. L.; et al. Liquids with high compressibility. *Adv. Mater.* **2023**, *35* (44), 2306521.
- (26) Fairen-Jimenez, D.; Moggach, S.; Wharmby, M.; Wright, P.; Parsons, S.; Duren, T. Opening the gate: framework flexibility in ZIF-8 explored by experiments and simulations. *J. Am. Chem. Soc.* **2011**, *133* (23), 8900–8902.
- (27) Wieme, J.; Vanduyfhuys, L.; Rogge, S.; Waroquier, M.; Van Speybroeck, V. Exploring the flexibility of MIL-47 (V)-type materials using force field molecular dynamics simulations. *J. Phys. Chem. C* **2016**, *120* (27), 14934–14947.
- (28) Rogge, S. M.; Wieme, J.; Vanduyfhuys, L.; Vandenbrande, S.; Maurin, G.; Verstraelen, T.; Waroquier, M.; Van Speybroeck, V. Thermodynamic insight in the high-pressure behavior of UiO-66: effect of linker defects and linker expansion. *Chem. Mater.* **2016**, *28* (16), 5721–5732.
- (29) Iacomini, P.; Lee, J. S.; Vanduyfhuys, L.; Cho, K. H.; Fertey, P.; Wieme, J.; Granier, D.; Maurin, G.; Van Speybroeck, V.; Chang, J.-S.; Yot, P. G. Crystals springing into action: metal-organic framework CUK-1 as a pressure-driven molecular spring. *Chem. Sci.* **2021**, *12* (15), 5682–5687.
- (30) Holden, D.; Jelfs, K. E.; Trewin, A.; Willock, D. J.; Haranczyk, M.; Cooper, A. I. Gas diffusion in a porous organic cage: analysis of dynamic pore connectivity using molecular dynamics simulations. *J. Phys. Chem. C* **2014**, *118* (24), 12734–12743.
- (31) Redfern, L. R.; Farha, O. K. Mechanical properties of metal-organic frameworks. *Chem. Sci.* **2019**, *10* (46), 10666–10679.
- (32) Redfern, L. R.; Robison, L.; Wasson, M. C.; Goswami, S.; Lyu, J.; Islamoglu, T.; Chapman, K. W.; Farha, O. K. Porosity dependence of compression and lattice rigidity in metal-organic framework series. *J. Am. Chem. Soc.* **2019**, *141* (10), 4365–4371.
- (33) Kresse, G.; Hafner, J. Ab initio molecular dynamics for liquid metals. *Phys. Rev. B* **1993**, *47* (1), 558–561.
- (34) Kresse, G.; Hafner, J. Ab initio molecular-dynamics simulation of the liquid-metal-amorphous-semiconductor transition in germanium. *Phys. Rev. B* **1994**, *49* (20), 14251–14269.
- (35) Vogel, D. J.; Rimsza, J. M.; Nenoff, T. M. Prediction of Reactive Nitrous Acid Formation in Rare-Earth MOFs via ab initio Molecular Dynamics. *Angew. Chem.* **2021**, *133* (20), 11615–11623.
- (36) Vogel, D. J.; Nenoff, T. M.; Rimsza, J. M. Tuned hydrogen bonding in rare-earth metal-organic frameworks for design of optical and electronic properties: an exemplar study of Y-2, 5-dihydroxyterephthalic acid. *ACS Appl. Mater. Interfaces* **2020**, *12* (4), 4531–4539.
- (37) Sava Gallis, D. F.; Vogel, D. J.; Vincent, G. A.; Rimsza, J. M.; Nenoff, T. M. NO<sub>x</sub> Adsorption and optical detection in Rare Earth Metal-Organic Frameworks. *ACS Appl. Mater. Interfaces* **2019**, *11* (46), 43270–43277.
- (38) Vogel, D. J.; Sava Gallis, D. F.; Nenoff, T. M.; Rimsza, J. M. Structure and electronic properties of rare earth DOBDC metal-organic-frameworks. *Phys. Chem. Chem. Phys.* **2019**, *21* (41), 23085–23093.
- (39) Rimsza, J.; Nenoff, T. M. Design of enhanced porous organic cage solubility in Type 2 porous liquids. *J. Mol. Liq.* **2023**, *377*, 121536.
- (40) Rimsza, J. M.; Chapman, K. W.; Nenoff, T. M. Energetics and structure of Ag-water clusters formed in mordenite. *J. Phys. Chem. C* **2020**, *124* (8), 4517–4524.
- (41) Rimsza, J. M.; Chapman, K. W.; Nenoff, T. M. Influence of Al location on formation of silver clusters in mordenite. *Microporous Mesoporous Mater.* **2021**, *327*, 111401.
- (42) Perdew, J. P.; Ruzsinszky, A.; Csonka, G. I.; Vydrov, O. A.; Scuseria, G. E.; Constantin, L. A.; Zhou, X.; Burke, K. Restoring the Density-Gradient Expansion for Exchange in Solids and Surfaces. *Phys. Rev. Lett.* **2008**, *100* (13), 136406.
- (43) Grimme, S.; Antony, J.; Ehrlich, S.; Krieg, H. A consistent and accurate ab initio parametrization of density functional dispersion correction (DFT-D) for the 94 elements H-Pu. *J. Chem. Phys.* **2010**, *132* (15), 154104.
- (44) Miklitz, M.; Jiang, S.; Clowes, R.; Briggs, M. E.; Cooper, A. I.; Jelfs, K. E. Computational screening of porous organic molecules for xenon/krypton separation. *J. Phys. Chem. C* **2017**, *121* (28), 15211–15222.
- (45) Jackson, E.; Miklitz, M.; Song, Q.; Tribello, G. A.; Jelfs, K. E. Computational evaluation of the diffusion mechanisms for C8 aromatics in porous organic cages. *J. Phys. Chem. C* **2019**, *123* (34), 21011–21021.
- (46) Hasell, T.; Culshaw, J. L.; Chong, S. Y.; Schmidtman, M.; Little, M. A.; Jelfs, K. E.; Pyzer-Knapp, E. O.; Shepherd, H.; Adams, D. J.; Day, G. M.; Cooper, A. I. Controlling the crystallization of porous organic cages: molecular analogs of isorecticular frameworks using shape-specific directing solvents. *J. Am. Chem. Soc.* **2014**, *136* (4), 1438–1448.
- (47) Le Roux, S.; Jund, P. Ring statistics analysis of topological networks: New approach and application to amorphous GeS<sub>2</sub> and SiO<sub>2</sub> systems. *Comput. Mater. Sci.* **2010**, *49* (1), 70–83.

(48) Vogel, D. J.; Lee, Z. R.; Hanson, C. A.; Henkelis, S. E.; Smith, C. M.; Nenoff, T. M.; Dixon, D. A.; Rimsza, J. M. Predictive Acid Gas Adsorption in Rare Earth DOBDC Metal-Organic Frameworks via Complementary Cluster and Periodic Structure Models. *J. Phys. Chem. C* **2020**, *124* (49), 26801–26813.

(49) Gould, N. S.; Li, S.; Cho, H. J.; Landfield, H.; Caratzoulas, S.; Vlachos, D.; Bai, P.; Xu, B. Understanding solvent effects on adsorption and protonation in porous catalysts. *Nat. Commun.* **2020**, *11* (1), 1–13.

(50) Katsoulidis, A. P.; Antypov, D.; Whitehead, G. F.; Carrington, E. J.; Adams, D. J.; Berry, N. G.; Darling, G. R.; Dyer, M. S.; Rosseinsky, M. J. Chemical control of structure and guest uptake by a conformationally mobile porous material. *Nature* **2019**, *565* (7738), 213–217.

(51) Henkelman, G.; Uberuaga, B. P.; Jónsson, H. A climbing image nudged elastic band method for finding saddle points and minimum energy paths. *J. Chem. Phys.* **2000**, *113* (22), 9901–9904.

(52) Henkelman, G.; Jónsson, H. Improved tangent estimate in the nudged elastic band method for finding minimum energy paths and saddle points. *J. Chem. Phys.* **2000**, *113* (22), 9978–9985.

(53) Hahn, S. H.; Rimsza, J.; Criscenti, L.; Sun, W.; Deng, L.; Du, J.; Liang, T.; Sinnott, S. B.; Van Duin, A. C. Development of a ReaxFF reactive force field for NaSiO<sub>x</sub>/water systems and its application to sodium and proton self-diffusion. *The Journal of Physical Chemistry C* **2018**, *122* (34), 19613–19624.

(54) Rimsza, J.; Yeon, J.; Van Duin, A.; Du, J. Water interactions with nanoporous silica: comparison of ReaxFF and ab initio based molecular dynamics simulations. *J. Phys. Chem. C* **2016**, *120* (43), 24803–24816.

(55) Egleston, B. D.; Luzyanin, K. V.; Brand, M. C.; Clowes, R.; Briggs, M. E.; Greenaway, R. L.; Cooper, A. I. Controlling gas selectivity in molecular porous liquids by tuning the cage window size. *Angew. Chem., Int. Ed.* **2020**, *59* (19), 7362–7366.

(56) Christian, M. S.; Hurlock, M. J.; Nenoff, T. M.; Rimsza, J. M. CO<sub>2</sub> adsorption mechanisms at the ZIF-8 interface in a Type 3 porous liquid. *J. Mol. Liq.* **2024**, *395*, 123913.

(57) Chen, L.; Che, Y.; Cooper, A. I.; Chong, S. Y. Exploring cooperative porosity in organic cage crystals using in situ diffraction and molecular simulations. *Farad. Disc.* **2021**, *225*, 100–117.